

CHAPTER II

GENERAL EXPERIMENTAL TECHNIQUES

A. Introduction

An overall schematic of the experimental apparatus is shown in Fig. 2.1. The apparatus comprises a flowing afterglow ion source coupled to a drift tube and has undergone continual modifications since its inception.¹ A goodly majority of the current incarnation of the apparatus is identical with a previous configuration, and is discussed in further detail in the thesis of Michael Bastian.² Substantive differences and important points for this work are discussed in the following sections. Section II.B covers ion production conditions and details of the flow-drift portion of the apparatus. The details of the ring dye laser system and relevant diagnostics are discussed in Sec. II.C. The detection of both unpolarized and polarized fluorescence is discussed in Sec. II.D. Sections II.E and II.F cover the necessary electronics and data acquisition programming, and some minor details of data analysis. Details of the spectroscopy of the $(v', v'') = (0, 0)$ band of the $N_2^+ B^2\Sigma_u^+ - X^2\Sigma_g^+$ system are discussed in Sec. II.G.

B. Ion source & flow-drift region

Because proper ion production and charge-separation conditions are essential to the correct measurement of transport properties, a brief discussion is given of these issues in this section. The ion are generated by a traditional flowing afterglow; ion production details are discussed in Sec. II.B.1. A brief discussion of the relevant

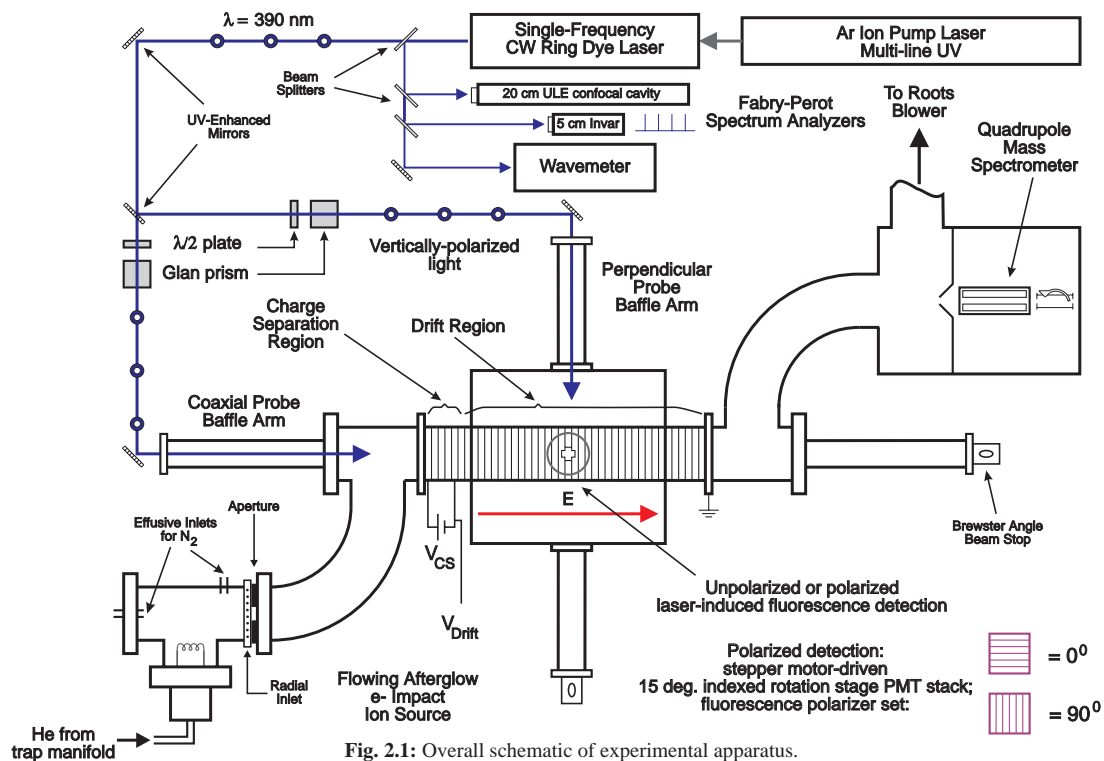


Fig. 2.1: Overall schematic of experimental apparatus.

hydrodynamics of the flow tube is presented in Sec. II.B.2. Sec. II.B.3 discusses the drift region of the apparatus.

1. Ion source & production conditions

The flowing afterglow characteristics are dominated by the buffer gas, which is helium for all work presented here. Approximately 5.1×10^{21} atoms s^{-1} , corresponding to a typical flow rate of 11.4 standard liters min^{-1} (slm), of industrial-grade He (nominal 99.995% purity) is passed through two liquid-nitrogen cooled cold traps containing 5 Å molecular sieves. The traps are pumped on and baked out continuously when not in use by custom heating mantles (Glas-Col) regulated by an autotransformer. The He flow rate is regulated by a mass flow controller (Tylan FC-280). The controller calibration, which is important for determining the bulk flow velocity of the buffer gas, can be checked with a wet test meter (Precision Scientific), as discussed more below.

The helium buffer then flows over an electron impact ion source, as detailed in Fig. 2.2. The ion source consists of a thoriated iridium filament, with a repeller plate directly behind and fine mesh grid directly in front of the filament. The entire source is covered by a slotted metal cup. Construction details of the filament and ion source are given in Bastian.² The ion source is biased by regulated voltage and current supplies (Kepco) that float with respect to the tube voltages. For all work presented here, the ion source was configured as an electron gun, in which the filament is biased at a voltage V_G that is negative relative to the “local ground”, (i.e., the ion source flange). Electrons are boiled off the filament by a filament current I_F (with associated

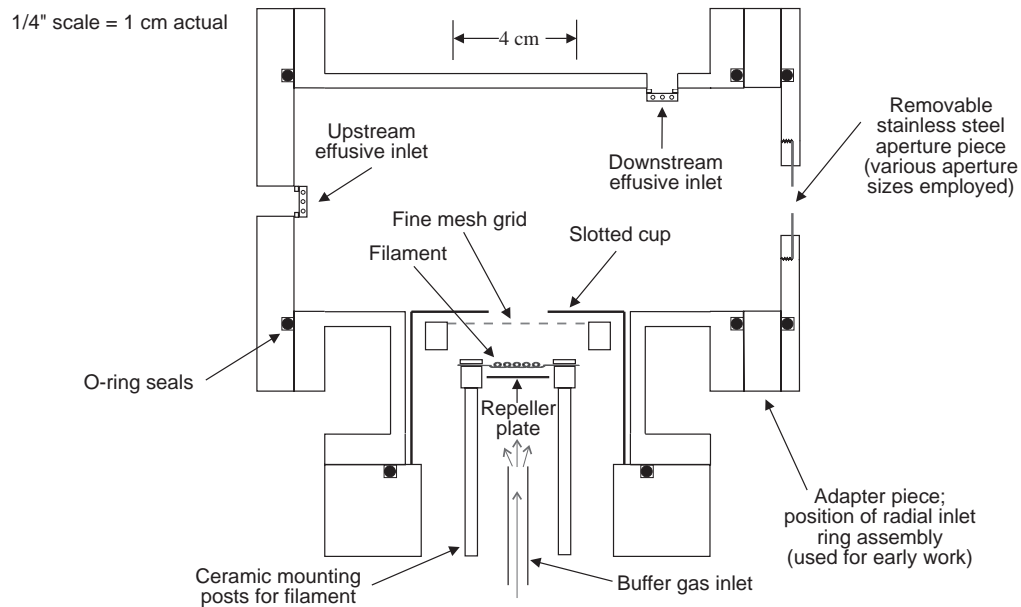
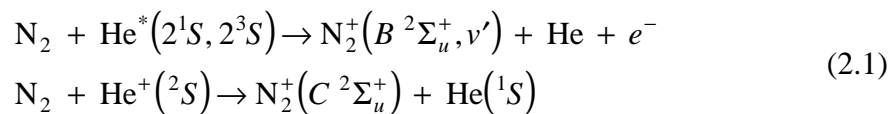


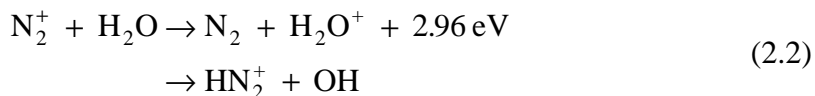
Fig. 2.2: To-scale diagram of ion source region. Electrical connections are shown schematically in Fig. 2.5 (after Ref. 2).

ohmic drop V_F), maintained at a value by the regulated current supply such that the emission current I_E collected by the mesh grid is held to a constant value, chosen by a potentiometer. For the electron gun configuration, the repeller plate is held at approximately $-V_G$ by tying it to the negative end of the filament. The fine mesh grid and slotted cup are at the potential of the source flange, which is in turn floated on top of the charge separation and drift voltage power supplies, as discussed below. Gas inlets for the buffer and neutral reagent gases are electrically insulated by glass tube and Cajon connector assemblies.

Because the cross sections for direct electron impact ionization for most small molecules are considerably less than the reactive cross sections at electron energies of 1-100 eV, the desired ions in a flowing afterglow are invariably formed through some sort of ion-molecule reaction. The dominant production reactions for $N_2^+(v'' = 0)$ are Penning ionization by metastable singlet and triplet helium and charge transfer with singly-ionized helium:^{3,4}



The singlet He metastable state is known to be efficiently quenched by superelastic electronic collisions in the afterglow,⁵ so the triplet state is assumed to be the dominant Penning ionization production channel. The primary loss mechanism for N_2^+ is the exothermic charge-transfer reaction with H_2O :



that accumulates in the tube or starts desorbing from the traps as they get saturated; the production of HN_2^+ is a secondary loss channel.

Although considerable time was spent searching for optimal production conditions, a small number of conditions were actually used in practice for the data presented here. Ion production conditions are monitored by a quadrupole mass spectrometer (Extranuclear/Extrel) located downstream of the flow-drift region, as shown in Fig. 2.1. Mass spectra were taken every time the experiment was run to monitor the production conditions and the cleanliness of the drift tube. Details of this particular ion detection system are given by Zwier,¹ Smith,⁶ Hamilton,⁷ and Bastian;² since just qualitative information was extracted from the mass spectra for this work, the mass spectrometer will not be discussed further.

The production condition mass spectra used for the two major sets of experiments in this work conducted in the Fall of '95 and the Fall '97/Spring '98 are shown in Figs. 2.3 and 2.4, respectively. The figure captions detail the specific conditions used. For the majority of the work, neutral N_2 alone was added via the upstream effusive inlet shown in Fig. 2.2; some early work was done by adding neutral Ar through this inlet, and neutral N_2 through the radial inlet ring whose position is shown in this figure. The flows of neutral reagents are monitored by mass flow meters (Tylan FM-360V) and regulated by needle valves. The removable stainless steel aperture in the source region 9 cm downstream of the filament increases the residence time of the gases in the source region to help drive the ion chemistry to completion before the drift region. Additionally, it was found that both the measured

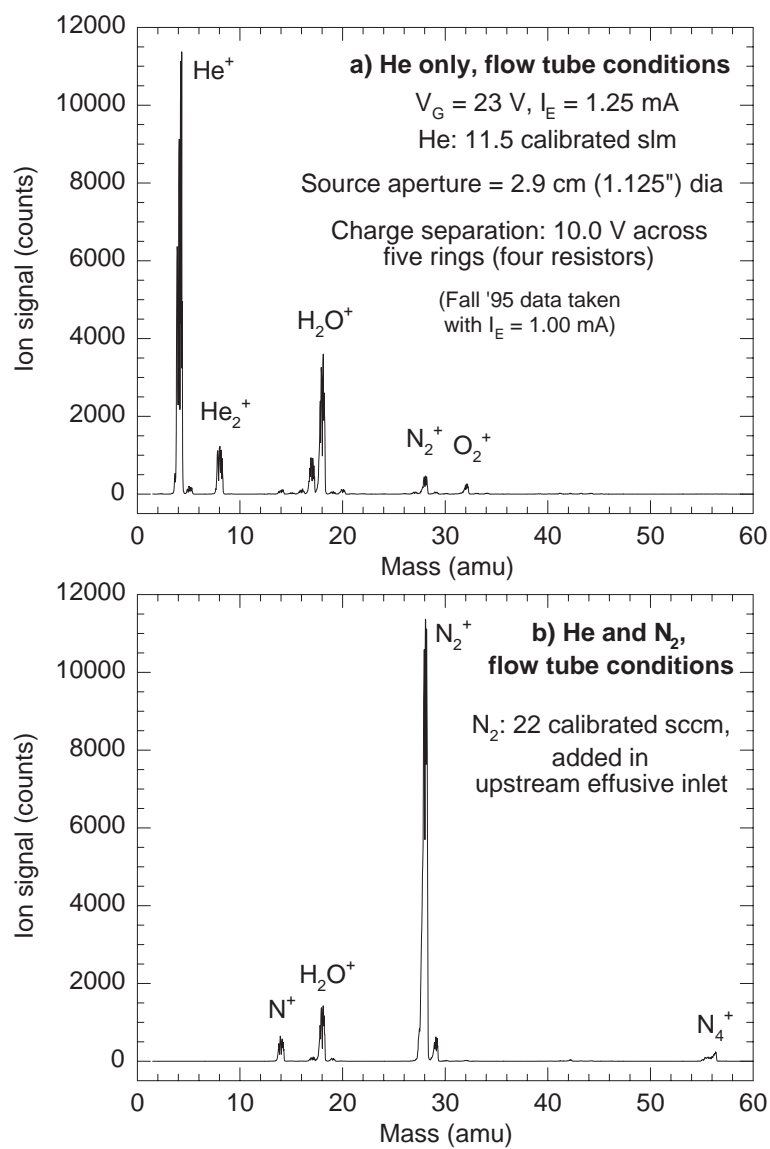


Fig. 2.3: Representative mass spectra for Fall '95 experiments.

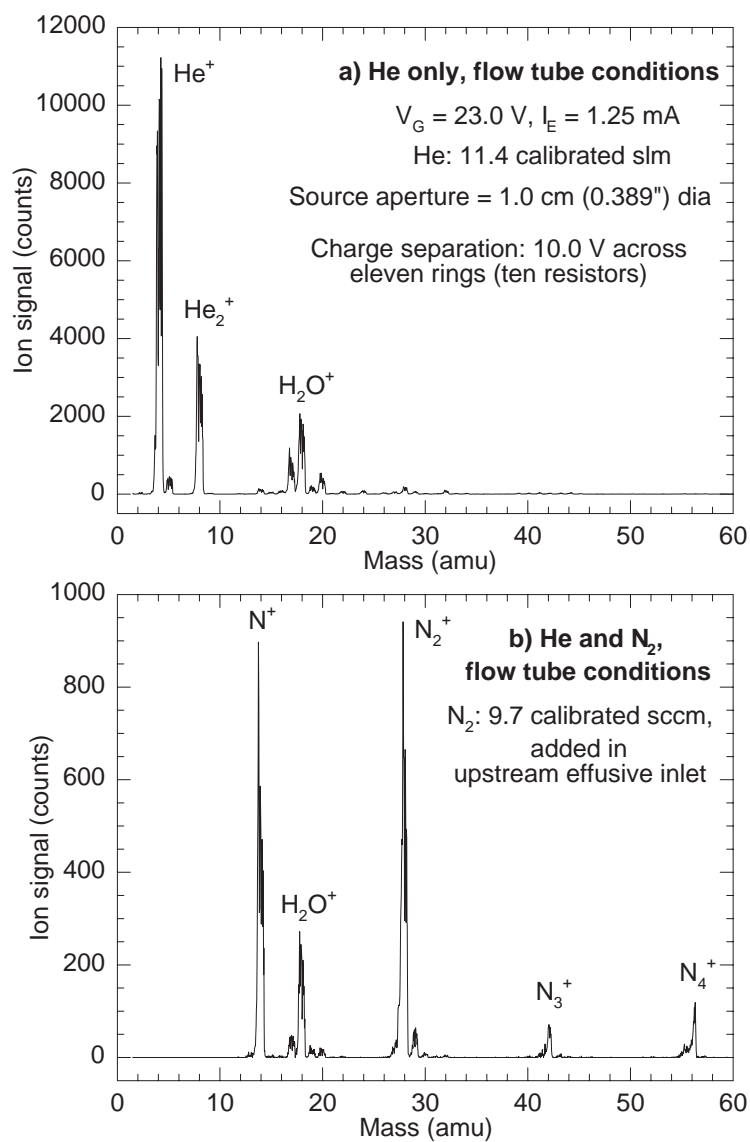
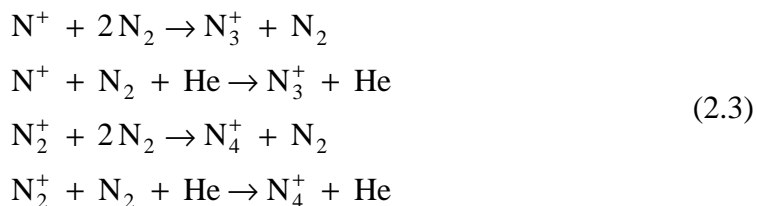


Fig. 2.4: Representative mass spectra for Fall '97 and Spring '98 experiments.

axial ion flow velocity and the apparent measured ion mobilities were greatly affected by the aperture size, as discussed in detail in Sec. III.E. Note that the conditions of Fig. 2.4 employ a substantially smaller aperture size; the presence of N_3^+ and N_4^+ in the lower panel of Fig. 2.4 is due to three-body reactions, such as



which proceed more efficiently in the higher pressure of the ion source under these conditions. Note that for cw LIF work, it is particularly important to choose production conditions that quench the flowing afterglow fluorescence, which is primarily due to collisional deactivation of $He(2^3S)$ with various buffer gas impurities such as H_2O and O_2 .⁵ The addition of neutral N_2 in the source region efficiently quenches this fluorescence.

As the above discussion indicates, a clean, dry flow-drift apparatus is a prerequisite for successfully making ions of reactive species such as N_2^+ . It was found helpful to wrap the source elbow, upstream and downstream tee's and all baffle arms with heating tape and "bake out" these regions between runs of experiments. Unfortunately, not all regions of the apparatus were accessible for baking; in particular, the Teflon rods and mylar spacers in the drift LIF assembly tend to trap water and cannot be baked out effectively. The best mass spectra were obtained when the apparatus was not vented for months and thus never exposed to atmosphere. Venting frequently would noticeably affect ion yield both in the mass spectra and in the LIF signal. Additionally, when running, it was found important to keep the trap

dewars full of liquid nitrogen to prevent water from desorbing from the top of the traps and accumulating in the tube.

2. Flow tube considerations

The flow tube (i.e., the portion of a flow-drift apparatus with no applied fields) is a flowing system dominated by the buffer gas behavior. A brief discussion is given of the relevant hydrodynamics of the flow tube portion of the apparatus, focusing on relations important for arguments given later in Chapter III.

The bulk or “plug flow” velocity v_0 of the buffer gas is linearly related to the buffer gas throughput Q_{buffer} and is given by⁸

$$v_0 = \frac{Q_{buffer}}{\pi a^2} \times \frac{760 \text{ Torr/atm}}{P(\text{Torr})} \times \frac{T(\text{K})}{273.16 \text{ K}} \quad (2.4)$$

where v_0 is in cm s^{-1} , Q_{buffer} is in $\text{atm cm}^3 \text{ sec}^{-1}$ and a is the radius of the flow tube in cm. With $a = 3.65 \text{ cm}$ for this apparatus, and expressing Q_{buffer} in the more convenient units of standard liters min^{-1} (slm), this gives

$$v_0 = 1.108 \times 10^{-2} Q_{buffer} \frac{T(\text{K})}{P(\text{Torr})} \quad (2.5)$$

with v_0 now expressed in m s^{-1} . Thus, if the He flow controller is calibrated with a wet test meter, the bulk velocity can be determined. For typical calibrated flow conditions of 11.4 slm of He at $P = 0.50 \text{ Torr}$ and $T = 298 \text{ K}$, v_0 is about 75 m s^{-1} . The buffer gas under laminar flow conditions will assume a parabolic velocity profile, with the velocity as a function of the radial position r from the tube axis given by^{8,9}

$$v(r) = 2v_0 \frac{\left[1 - (r/a)^2 + (2s/a)\right]}{\left[1 + (4s/a)\right]} \quad (2.6)$$

where $s = s'/P$ is the slip coefficient. For negligible buffer gas slip at the flow tube walls (i.e., $s/a = 0$), this reduces to

$$v(r) = 2v_0 \left[1 - (r/a)^2 \right] \quad (2.7)$$

Note in particular Eq. (2.6) predicts an on-axis ($r = 0$) buffer flow velocity of $2.0 v_0$ for no slip; for $s/a = 0.02$ (a couple percent slip), the axial flow velocity is about $1.9 v_0$. Thus, a well-behaved flow tube operating in the laminar flow regime should have a ratio of axial ion flow velocities to buffer gas bulk velocities of 1.9 to 2.0.

The conventional indicator of laminar/turbulent flow is the Reynolds number, given by

$$R_e = \frac{\rho v_0 a}{\eta} \quad (2.8)$$

where ρ is the buffer gas mass density in g cm^{-3} , v_0 is the buffer bulk flow velocity in cm s^{-1} , a is the tube radius in cm, and η is the buffer gas viscosity in poise ($\eta_{\text{He}} = 189.6 \times 10^{-6} \text{ P}$). For the typical conditions given above, $R_e \cong 16$, indicating that conditions are well within the laminar flow regime. The entry length, the minimum length needed to establish laminar flow, is given by

$$L_e = 0.227 a R_e \quad (2.9)$$

which gives an entry length of approximately 13 cm for typical conditions. The length of the flow region elbow alone shown in Fig. 2.1 is 28 cm. These calculations, along with calibration measurements discussed in Chapter III that consistently produce an axial ion flow velocity of 1.9 to 2.0 times the bulk flow in *flow tube* (zero-field) conditions, strongly suggest that the buffer gas flow in this apparatus is laminar and

well-behaved. In particular, the anomalous axial ion velocity systematics observed in *drift tube* conditions that are discussed in Chapter III are not believed to be due to turbulent flow or insufficient entry length.

3. Drift & charge separation regions

The resulting space-charge neutral plasma from the flowing afterglow source flows through a 44-cm-long field-free region to the drift region. An electrical schematic of the drift region and its relation to the source and flow regions is shown in Fig. 2.5. The drift region consists of a total of either 45 or 51 guard rings (depending on configuration; Fig. 2.5 shows the 51-ring apparatus), 1-cm-wide by 7.3-cm-i.d., electrically insulated by mylar spacers and connected in series by a network of precision 500 Ω vacuum resistors (Caddock). The resistor values are chosen to keep the network biasing current much larger than the ion recombination current at the walls. The entire drift assembly is held together by compression between two gold-plated aluminum flanges, as indicated in the figure. Two voltage supplies are used for the drift region. The charge separation supply, which floats on top of the drift voltage supply, is used to establish the charge separation field in the first portion of the drift region, as discussed further below. A drift voltage supply across the remaining guard rings is used to establish a uniform variable axial electric field in the drift region proper. The drift supply has its ground lead tied to the downstream flow region.

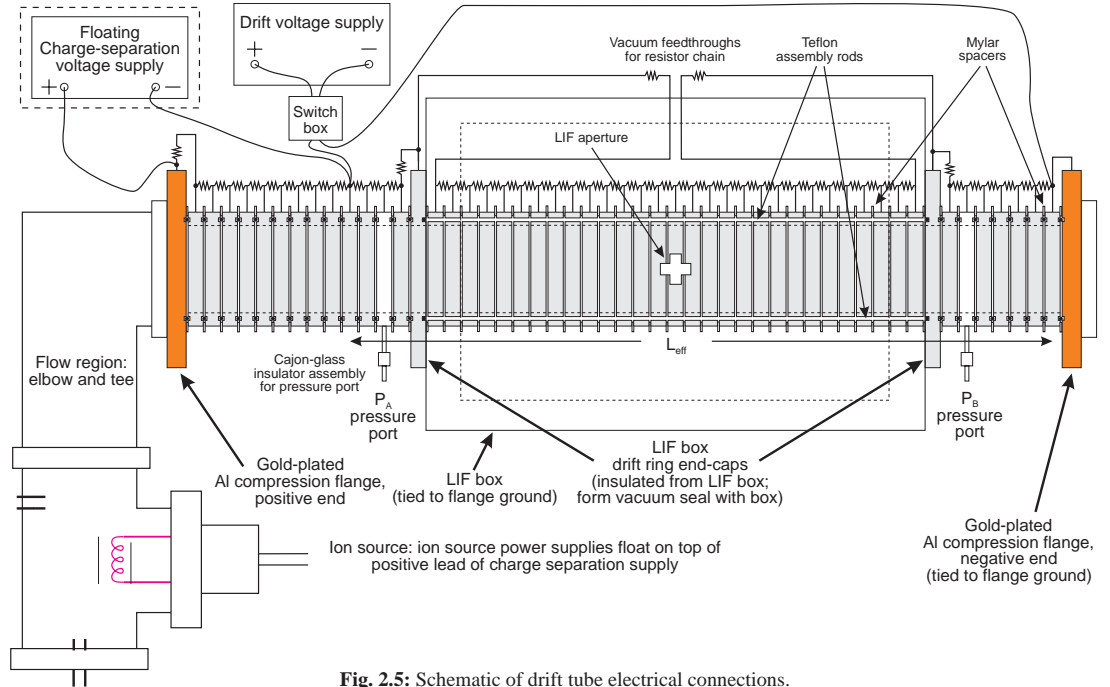


Fig. 2.5: Schematic of drift tube electrical connections.

In a drift tube apparatus, the field parameter is the ratio E/N of external applied electric field to buffer gas number density, conventionally measured in townsend (1 Td = 10^{-17} V cm²). A convenient conversion factor between E/N and E/P can be produced from the ideal gas law:

$$\frac{E}{N} = k_B T \frac{E}{P} \quad \text{or} \quad \left(\frac{E}{N} \right) = 1.0356 \times 10^{-2} T \left(\frac{E}{P} \right) \quad (2.10)$$

with E/N in Td, T in degrees Kelvin, and P in Torr. We desire a formula for E/N at the LIF imaging region of the drift tube, $(E/N)_{LIF}$. The external applied electric field is assumed to be the applied drift voltage across the drift region of the tube divided by the effective tube length, as measured from ring center to ring center. Simulations in *Simion* show this to be an excellent approximation for the axial field strength, and the field remains uniform to within 1% up to about 80% of the tube radius. P_{LIF} is determined by linear interpolation of readings taken at two pressure ports 17 cm up and downstream of the LIF region, as shown in Fig. 2.5. These ports are connected to a 1 Torr capacitance manometer (MKS Baratron), which is referenced to the quadrupole chamber pressure (effectively zero Torr). By convention, the tube pressure is measured downstream at port B and multiplied by a scale factor s to obtain the pressure at the LIF region. Taking then:

$$E_{LIF} = \frac{V_{drift}}{L_{eff}}, \quad P_{LIF} = s P_B, \quad T = T_{room}, \quad (2.11)$$

gives a field strength formula for E/N at the LIF region:

$$\left(\frac{E}{N} \right)_{LIF} = 1.0356 \times 10^{-2} \frac{V_{drift} T_{room}}{s P_B L_{eff}} \quad (2.12)$$

with E/N in Td, V_{drift} in volts, T_{room} in Kelvin, P_B in Torr and L_{eff} in cm. The room temperature is measured by a mercury thermometer adjacent to the apparatus. The pressure scaling factor must be empirically determined for each apparatus assembly. For the assembly used for the majority of this work, s was found to be 1.022 from repeated measurements of P_A and P_B . A typical running pressure P_B was about 0.4905 Torr. The effective tube length L_{eff} was 41 cm for this assembly.

To measure proper transport properties in a drift-tube apparatus, it is necessary to separate the negative species (primarily electrons) from the plasma to achieve a space-charge limited density of ions drifting in neutral buffer gas. A simple estimate produced from a one-dimensional Poisson's equation argument¹⁰ yields an upper bound of approximately 10^6 ions cm^{-3} for negligible space charge effects for the dimensions of this apparatus. The conventional way of insuring both these conditions is to create a charge separation region, consisting of a number of rings prior to the drift region proper that are maintained at a separate field strength than the drift region. Ideally, the charge separation region creates a barrier for all free electrons in the plasma, and one is left with a space-charge-limited density of positive ions alone in the drift region. Unfortunately, it was found that the apparent axial ion flow velocities can be significantly altered by the length and position of the charge separation region, probably indicating that the ion density is above the space charge limit. For the majority of the work presented here, the charge separation region consisted of 11 rings (10 resistors) with 10.0 V across these resistors for a nominal 1 V cm^{-1} external electric field; this configuration was found to minimize these effects. A discussion of

artifacts introduced by possible space-charge effects due to either too high ion density or free electrons is deferred to Sec. III.E.

The drift and LIF box assembly shown in Fig. 2.5 was cleaned and reconfigured several times in the course of this work; this assembly is non-trivial to disassemble, clean, and reassemble properly. It was found useful to construct blank-off flanges for the up and downstream compression flanges of the assembly so that it could be leak-checked as a unit with the JILA console leak detector. Typical quiescent final pressure one can achieve in a clean, dry, leakless system is 1.5×10^{-7} Torr or better in the quadrupole chamber.

C. Ring dye laser system & diagnostic tools

The resultant N_2^+ ions in the drift tube are probed by a single-frequency ring dye laser system, as discussed in this section. Ring dye “laserology” turns out to be particularly important for this experiment due to its inherent repetitiveness. Additionally, operating at and below 390 nm required using a near-UV dye that is costly, short-lived, and sometime difficult to achieve consistent results. It should be mentioned that if future experiments requiring a cw laser in this wavelength range are attempted, the acquisition of a Ti:Sapphire ring system and the construction of an *external* actively-stabilized doubling cavity with a BBO, LBO, or $LiIO_3$ crystal as a second-harmonic generation medium should be seriously considered.¹¹ The laser pump requirements would be in the visible (514 nm) and much less stringent. The additional power stability and reliability would permit longer scan times and more coadds. Lastly but not leastly, an all solid-state system would relieve some of the pain and suffering commonly associated with ring dye lasers, with which this investigator

is intimately familiar. This is an important consideration, as chemical physics experiments are becoming more complex, and single-frequency lasers are now often just one of several lasers employed in an experiment, used perhaps for intermediate-state preparation.¹²

1. General description

An optical and electronics schematic of the relevant portions of the ring dye laser system (Coherent 699-21) is shown in Fig. 2.6. The basic concepts of a moderate-resolution, actively-stabilized ring dye laser are well-described in the literature.¹³⁻¹⁵ Briefly, the laser consists of a vertically-folded ring cavity defined by four mirrors. A thin ribbon of dye jetted into the cavity serves as the lasing medium and is pumped by an argon ion laser. A hierarchy of three increasingly selective frequency elements (i.e., the birefringent filter, thin etalon, and thick etalon) force the laser to run in a single longitudinal cavity mode, with an actively-stabilized linewidth of less than 1 MHz. The scanning elements (α , β , χ , and γ in Fig. 2.6) are controlled by a cavity-side-lock system which employs a temperature and pressure stabilized confocal Fabry-Perot reference cavity with a free spectral range of 1.0 GHz. The electronics consist of essentially two servo loops. The air-spaced thick etalon is translationally tuned by a separate dither-and-track loop that keeps the thick etalon centered on the chosen longitudinal mode. The second servo loop is the cavity-side-lock that uses the reference cavity as a frequency discriminator. The reference cavity Brewster plate (δ) is scanned under either internal or external control and the scan is

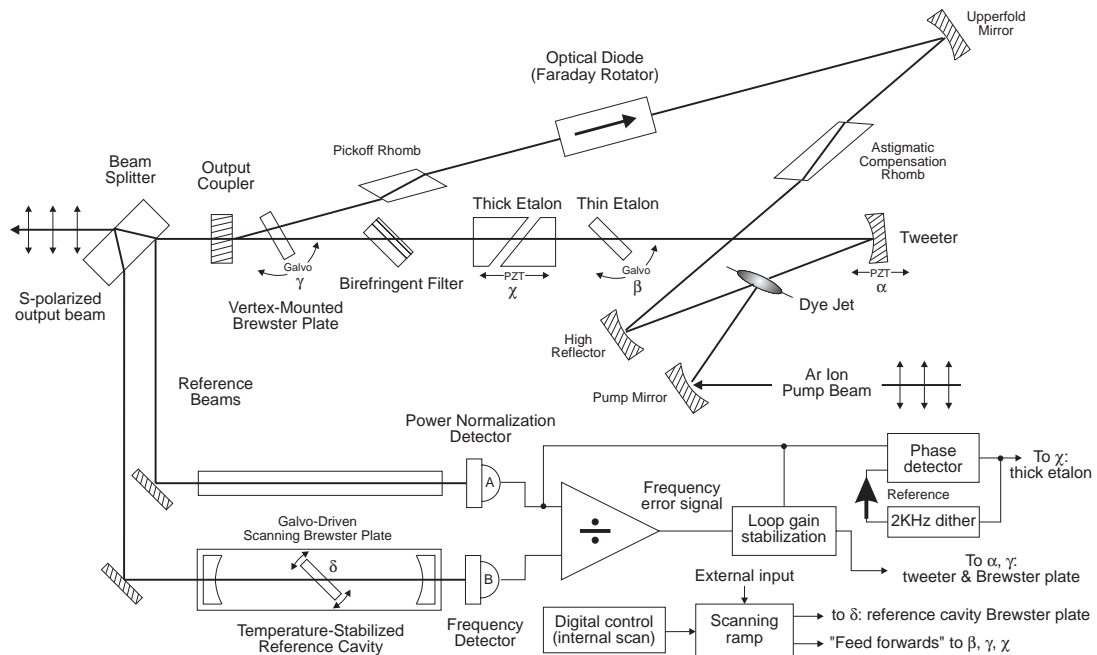


Fig. 2.6: Coherent 699-21 ring dye laser optical & electronics schematic.

fed-forward to the thick and thin etalons and intracavity Brewster plate (χ , β , and γ) to roughly position these tuning elements as the laser is scanned. Feed-back information derived from the reference cavity is used by the second servo loop to actively stabilize the laser by continuously positioning the fast (tweeter, α) and slow (Brewster plate, γ) intracavity elements to keep the frequency error signal at the lock point. These elements compensate primarily for dye jet jitter and air temperature and pressure perturbations to the cavity, respectively.

Dye preparation and use was (unfortunately) a significant practical consideration for this experiment due to the expense and short life of the dye. The dye used was Exalite 392E, a proprietary near-UV dye (Exciton Chemical Co.) with a molecular weight of 723 amu, and useful single-frequency spectral range of approximately 388 to 392 nm. Although significantly more robust than the polyphenyl dyes it was developed to replace,¹⁶ this dye still requires special preparation and handling. Recommended concentrations for CW ring dye laser use vary from 1.6 to 4.15 millimolar (mM) solutions of dye in ethylene glycol. Two grades of glycol were used over the course of this experiment (Mallinckrodt AR and Fisher Certified), both with a typical water content of 0.05% or less; glycol lots should always be chosen with the lowest water content available. Pragmatically, the dye recipe used for the majority of this work consisted of adding 3.00 g of pulverized dye to 300 ml of ethylene glycol to form a premix solution. The dye is supplied in microcrystalline form and must be crushed in a mortar and pestle to the consistency of talcum powder to insure that it goes systematically into solution. The premixes were prepared two at a time, sonicated and then mixed for at least 24 hours on a stirplate. After flushing the old dye from the jet system, 900 ml of glycol was added and the dye circulator

checked for leaks before adding the 300 ml of dye premix, resulting in a 3.46 mM operating solution. It should be pointed out that the only way to be certain of the correct dye concentration is to check the dye jet absorption of the pump beam as a function of dye solution molarity (80-85% absorption is optimal); this was done several times in the course of the work. The dye solution needs to be purged of microbubbles by circulating the dye at a low pressure for several hours. Ring dye laser output power will be dependent on jet operating pressure; it was found empirically that the highest pressure that can be reliably run without danger of foaming is 54 psi.

Exalite 392E is optimally pumped by the mid-UV lines (333.6 to 363.8 nm, “all lines”)¹⁷ generated by Ar^{2+} in an argon ion laser. Two large-frame argon ion pump lasers were used in the course of this work. The original pump laser (Coherent Innova 20) had a passively stabilized quartz crystal resonator structure which required continual reapeaking, noticeably affecting the beam-pointing stability. When the cathode sagged on the tube in this laser, a tube refurbishment procedure was attempted, with decidedly mixed results. With “20-20 hindsight”, it was recognized that the pump requirements for this experiment were probably too demanding to be met by a refurbished laser tube. The second pump laser (Coherent Innova 400) has an actively-stabilized Invar resonator; the ring dye laser output is noticeably more consistent and stable over time with this pump source. For near-UV dyes, the pump mode is very important for achieving optimal results; pump mode can be observed in the far field by splitting off a fraction of the pump beam with a simple beamsplitter and expanding it with a lens onto a white card. The “donut mode” (linear combination of TEM_{01} & TEM_{10} modes)¹⁸ is a particular and well-known problem with these lasers. These modes develop over time because of color centers formed on the

crystalline quartz Brewster windows of the laser tube. Donut modes can be eliminated by aperturing down intracavity, at the expense of output power. It was found that for this dye, optimal results were always achieved with larger pump mode volumes, even if these volumes included some “donuts”.

The highest single-frequency power achieved with this dye was 105 mW at the output coupler; a more typical running power is 80 mW with fresh dye. Dye lifetimes depend on several factors, including pump laser power and mode, ring cavity alignment, and cooling water temperature. A typical value is fifteen running hours to approximately one third of initial power. The dye solution will turn from clear when new, to pale straw, to a dark urine color when completely oxidized. For optimal dye lifetime, it was found necessary to eliminate all brass parts from the dye utility module and replace them with stainless steel. Additionally, it was found helpful to time dye use with a stop-watch in order to know the usable dye lifetime left, so that future experiments could be planned. The need to work quickly on the ring dye laser with this dye, to know when and when not to make compromises, and always, to be flexible in experiments performed cannot be overemphasized.

2. Diagnostic tools

The ring dye laser is used in conjunction with other diagnostic tools, as shown in the optics table schematic of Fig. 2.7. A fraction of the output beam from the laser is split off by a primary coated 85/15% beamsplitter (CVI Laser Corporation). This beamsplitter is sufficiently thick such that the secondary reflection off of the

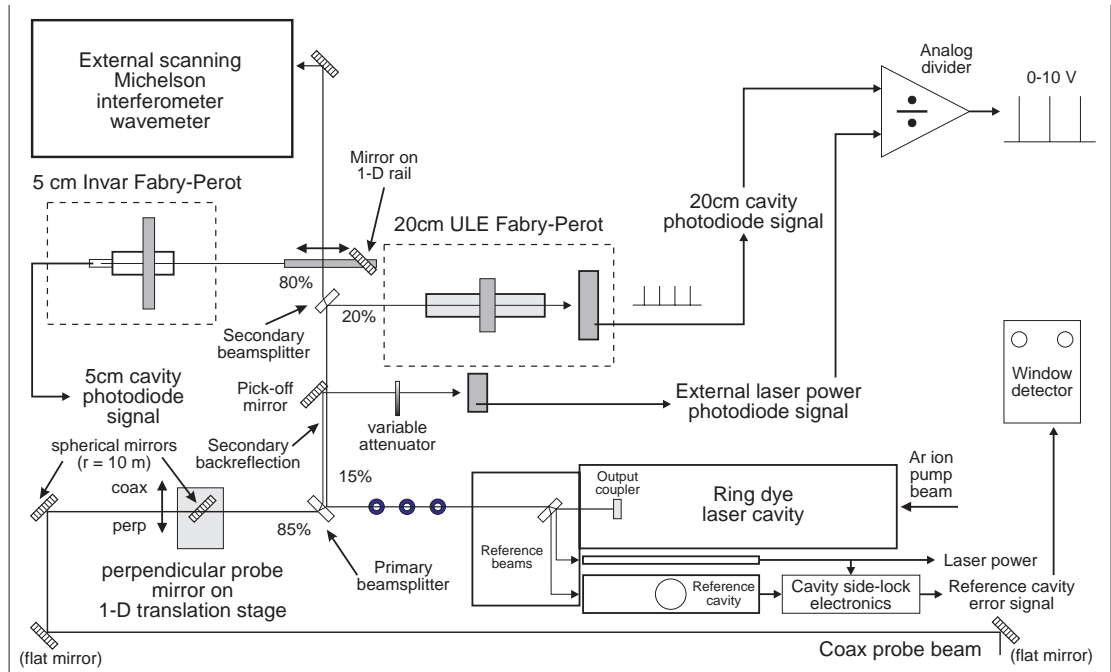


Fig. 2.7: Optics table schematic, showing ring dye laser and associated diagnostic tools.

nominally AR-coated back surface is spatially well-separated from the primary split-off beam. This secondary reflection was put to good use by directing it via a pick-off mirror to an external photodiode (EG&G FND-100Q), used as input to the laser power channel for the transport property experiments, and as the normalizing photodiode for the analog divider (discussed below) in the alignment experiments.

A second coated beamsplitter splits the primary diagnostic beam 80/20%. For typical data-taking conditions on the transport property experiment, these beams were directed to the two confocal Fabry-Perot spectrum analyzers used in the course of this work. One is a commercial Invar cavity (Coherent Model 240), 5 cm in length, with a free spectral range ($\text{FSR} = c/4L$) of 1.50 GHz. This cavity has a piezoelectric translator on the back mirror which enables the transmission fringes to be tuned or dithered in frequency by applying either a DC voltage or a ramp. A simple “high-voltage” piezo ramper was constructed to exploit this capability (schematic in JILA electronics shop). This proved quite useful; the consistently downward slope of laser power with time meant that with each dye change, inevitably there would be a point at which not enough power was available to obtain an external wavemeter reading. The 5 cm long Invar cavity could then be used as an *ad hoc* wavemeter. The laser beam is multiplexed quickly between the wavemeter and the Fabry-Perot cavity by a simple mirror mounted on a 1-D translation rail.

Although convenient to use at times, the commercial 5 cm Invar cavity is not particularly stable in frequency. Also, its relatively long free spectral range means that few frequency markers appear in the framing of a short laser scan; a cavity with a shorter FSR was desired in order to compute scan widths more accurately for the transport property experiments. Additionally, a stable frequency marker cavity was

needed for the sub-Doppler alignment experiment. For these reasons, a simple “ultrastable” confocal Fabry-Perot cavity, 20 cm in length, with a free spectral range of 0.375 GHz was constructed, as diagrammed in Fig. 2.8. The cavity mirrors are two stock plano-concave spherical mirrors (CVI Laser Corporation) of 20.0 cm radius and a surface figure of $\lambda/10$, with a reflectivity of 99.5% over the wavelength range 388 to 392 nm. A ultra-low thermal expansion (Corning “ULE”) titanium silicate glass¹⁹ cylindrical piece of indicated dimensions was bored and countersunk by the JILA instrument shops. The ULE cylinder was mounted in a JILA lens mount, and the mirrors were arranged perpendicular to the bore. The mirror spacing was adjusted to maximize finesse, and the mirrors affixed to the ULE with Torr-Seal, following the construction technique of Hall labs.²⁰ Note that the mirror holes and cavity should be completely sealed immediately to prevent debris from migrating into the cavity and destroying the reflectivity finesse (this initially occurred with this cavity). A simple photodiode circuit was constructed to detect the transmission fringes.

A scope trace of the 20 cm ULE cavity’s transmission fringes, with the 5 cm Invar cavity fringes shown for comparison, is given in Fig. 2.9. The total instrument finesse may be estimated from such a diagram; the finesses are approximately 100 and 25 for the 5 cm Invar and 20 cm ULE cavities, respectively. Because the performance of the ULE spectrum analyzer in a reasonably draft-free room was adequate for these purposes, no attempt was made to temperature-stabilize it. However, it was found important to construct plexiglass boxes around both cavities to minimize convective temperature cycling. The coefficient of thermal expansion of

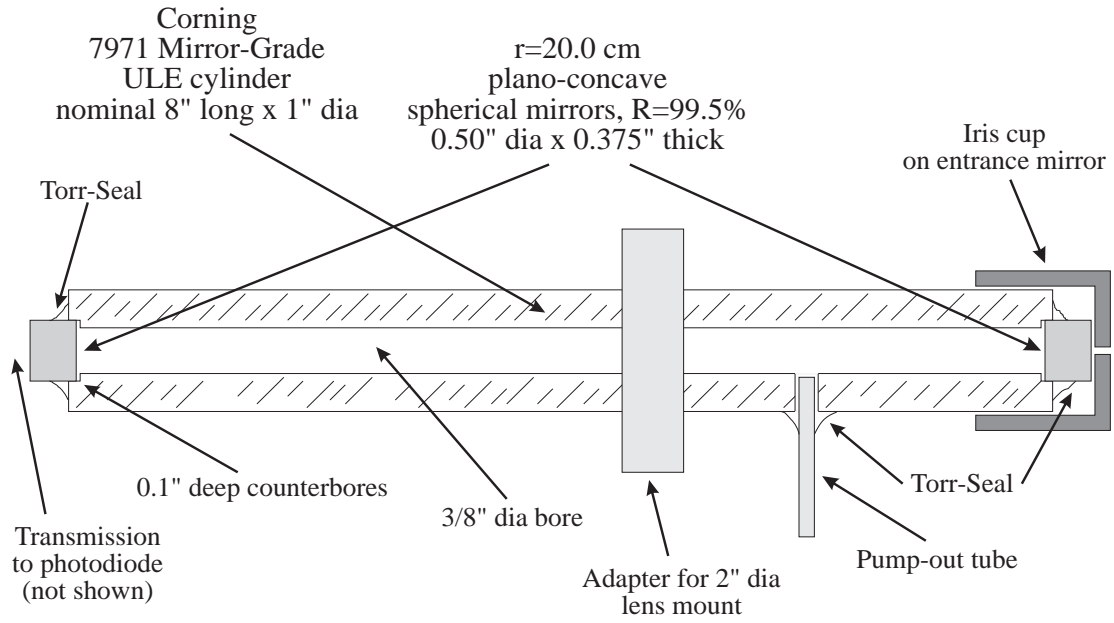


Fig. 2.8: Construction schematic of 20 cm ULE confocal Fabry-Perot cavity.

ULE is specified as $\alpha_{ULE} = 0 \pm 30 \times 10^{-9} / ^\circ C$, with a maximum variation of 15 ppb per degree C in a boule of material. A simple analysis with these numbers give a thermal shift in frequency of a transmission fringe of approximately $20 \text{ MHz } ^\circ C^{-1}$. The constructed ULE cavity is considerably less stable than this figure would imply primarily due to its low thermal mass. With a density $\rho_{ULE} = 2.21 \text{ g cm}^{-3}$ and a specific heat $c_{ULE} = 0.183 \text{ cal/g } ^\circ C$, the thermal mass of this cavity is approximately $36 \text{ cal } ^\circ C^{-1}$. Additional long-term frequency stability could undoubtedly be achieved by the construction of a simple “hot box” as a temperature stabilizer.

For the rotational alignment experiment, the 20 cm ULE cavity was used to generate frequency markers for sub-Doppler data acquisition. The reference cavity Brewster plate (δ in Fig. 2.6) can be simply modeled as a critically-damped oscillator driven by the internal or external scanning ramp (i.e., as a “screen door” pushed and pulled by the ramp). If a marker cavity such as this one is used as feedback to position the laser in frequency, and the external ramp simply stopped once the maximum of a transmission fringe appears, the reference cavity Brewster plate will overshoot the target position, and the laser frequency will end up in some unknown location between free spectral ranges. A simple scheme was adopted to get around this problem. An analog divider circuit which mimics the electronics of a cavity-side-lock system was constructed (schematic in appendix A) to divide out the laser power dependence of the cavity transmission and to insure that each transmission peak is the same amplitude. The numerator input is the 20 cm ULE cavity photodiode and the denominator input the aforementioned laser power photodiode. The output is a 0-to-10 V signal sampled by the microcomputer’s analog-to-digital converter. Two

empirically-determined voltage thresholds are used in conjunction with a simple step-and-sample algorithm in the acquisition program (Eta-Spex) to position the laser frequency onto an arbitrary cavity transmission fringe. One voltage threshold is used simply to count passing fringes as the laser is slewed. Once the fringe immediately prior to the target fringe has appeared, the slew rate is slowed and the threshold lowered. The external ramp is then stopped as soon as this lower voltage threshold is reached; the additional “creep” of the Brewster plate alone will consistently position the laser frequency above 80% of fringe peak height in under a second. False fringes caused by noise or the laser coming momentarily out of lock can be easily discriminated against by keeping track of the fringe width. Although this scheme works remarkably well in practice for the relatively coarse (± 30 MHz) frequency positioning needs of this experiment, because the 20 cm ULE cavity is still quite unstable, no attempt was made to transfer the frequency lock to this cavity.

Although the Fabry-Perot spectrum analyzers are useful for scan width analysis and frequency positioning within a scan width, a spectrometer of some sort is needed to make rotational line identifications. The external scanning Michelson interferometer wavemeter employed here (Burleigh Model WA-20) has an absolute accuracy of ± 0.001 nm, and its resolution of ± 0.01 cm^{-1} is sufficient to distinguish between thick etalon modes of the ring laser. The wavemeter was usually not employed for the transport property experiments once the desired LIF transition was found. For the sub-Doppler alignment experiments, the wavemeter was useful as a diagnostic while running (if sufficient power was available) to verify the laser had not mode-hopped during a data acquisition sequence.

A rough diagnostic of how well the ring dye laser was running on a particular day could be obtained by counting how frequently the cavity-side-lock servo loop broke lock due to microbubbles in the dye stream, dye jet pressure fluctuations, or environmental perturbations. Note that the presence of microbubbles in the dye stream (a particular problem for single-frequency operation) can be detected by looking for sharp downward transitions on the laser power channel. Each time the servo loop breaks lock, the intracavity Brewster plate (γ in Fig. 2.6) will attempt to compensate. If too much error accumulates such that the Brewster plate will tip out of range if it attempts to compensate for additional cavity length variations, a galvo recentering circuit automatically breaks lock and recenters the Brewster plate. These recenterings are undesirable, as they will often induce a longitudinal mode hop while all servo loops are open. To monitor the number of unlock/lock transitions, a simple window detector circuit (schematic in appendix A) was constructed to detect and count these transitions. The input of the detector is the reference cavity error signal, and its output is a logic-level pulse, one for each transition. Front-panel LED's provide additional visual cues, which are very convenient for monitoring across the room, as the rapid scope transitions cannot be seen from a distance. Discriminator levels were arbitrarily set at $\pm 1V$ above the lock point (ground) to count the largest, slowest unlock/lock transitions, which lead to the most rapid accumulation of Brewster plate error. Although originally constructed for the alignment work, the window detector proved so useful in practice that it was used constantly.

Lastly, note that for a Coherent 699-21, both the intracavity Brewster plate and thick etalon error signals are accessible for diagnostic purposes. The thick etalon error signal can be monitored directly from the back-panel of the ring dye laser control box.

This signal was monitored continuously for both sets of experiments. A discontinuity in the thick etalon error signal usually reflects a mode hop, as the etalon is now being dithered about a different longitudinal mode, and monitoring the signal can be an immediate way to determine this. The intracavity Brewster plate error signal is displayed on the front-panel of the ring dye laser control box, and can be monitored internally at TP5 of the 1A9 circuit board; if the voltage at this test point exceeds $\pm 0.9\text{V}$ (corresponding to 80 to 20 μA on the front-panel meter), the galvo will recenter.

3. Beam transport & polarization control

The output laser beam is transported to the apparatus table and into the baffle arms by a set of mirrors, as shown in Figs. 2.1 and 2.7. Two mirrors were needed for the perpendicular laser probe direction, and three for parallel (coaxial) probe. The mirror sets were independent, and the probe directions could be easily switched by sliding into place or aside the first perpendicular probe mirror, which was mounted on a 1-D translation stage, as shown in Fig. 2.7. The ability to quickly toggle between the two probe directions was particularly important for measuring axial ion flow velocities, as discussed in Sec. III.E. Unfortunately, mirrors with ordinary (i.e., uncoated, oxidized) aluminum surfaces will have losses of 50% or greater per mirror at $\lambda \leq 390\text{ nm}$. Special “UV-enhanced” aluminum mirrors with MgF_2 dielectric coatings (Melles Griot, coating code 028) were employed to keep mirror losses at a tolerable 2 to 5% level. The baffle arm entrance windows were fused silica and mounted between two O-rings to minimize strain and avoid possible stress-induced birefringent effects. The exit baffle arms are terminated in Brewster-angle window beamstops that were rotated into the plane of the dominant polarization sense of the probe beam (usually vertical).

To aid in the beam transport, drilled table extensions were constructed for the apparatus table and a breadboard assembly made for the coaxial probe baffle arm. Additionally, counterpropagating HeNe laser beams were employed in each probe direction to get the beam transport near-perfect and thus minimize background contributions from scattered laser light. The HeNe lasers were mounted behind the Brewster-angle windows and were prealigned with the aid of a target that fit into the baffle arms. Once aligned, the HeNe beams allowed the investigator to iterate through the set of mirrors for a given probe direction very quickly to get the ring dye laser beam alignment close to optimal. Fine adjustment was always done by observing the PMT signal and comparing the scattered laser light levels with the PMT dark-count rate. The use of a multi-channel scalar (Nicolet) as a “stripchart” to check scattered laser light proved quite useful. It was particularly important for the alignment experiment to get the background contributions from scattered laser light as low as possible. As a residual beam-transport note, it was also found necessary to refrain from adjusting the lower fold mirror (tweeter) of the ring dye laser cavity once the laser was initially peaked with fresh dye. This intracavity mirror most affects the pointing of the output beam, and even a small adjustment of the tweeter would be magnified by the long beam throws of this experiment and noticeably perturb the beam transport.

The output beam of the ring dye laser is nominally vertically polarized; this s-wave polarization sense is preserved by the beam transport mirrors to the apparatus table. The transport property experiments did not necessarily require modification of the polarization state. For the rotational alignment experiments however, polarization control of the probe beam is crucial. A zero-order polymer half-wave plate

(Meadowlark Optics) with $\lambda_c=390$ nm was used to rotate the plane of polarization of the probe beam. Primarily, the half-wave plate was used as a compensator to match the “vertical” of the probe beam with the “vertical” of the fluorescence imaging axis and to correct for small polarization rotations that occur in the beam transport. A Glan-Taylor polarizing prism (Melles Griot) was used following the wave plate to insure linear polarization purity of the probe beam. Any residual elliptical polarization present in the incident beam, whether due to imperfect ring dye laser alignment, beam transport, or partial-wave retardation of the wave plate, will be extinguished by the Glan prism. Note in particular that Fig. 2.1 is somewhat misleading; there are no additional optics of any sort (besides the baffle arm entrance windows) after the polarization optics. The retardance of polymer wave plates is fairly insensitive to incident angle, so the wave plate was mounted in a simple one-axis rotary stage; the Glan prism was mounted in a three-axis rotary stage with separate tilt adjustments. For proper operation, both polarization optics must be aligned normal to the laser beam. This can be accomplished by locating the retro-reflection off the front surface of the optic and then adjusting the tilt of the optic to make the retro coincide with the incident beam. Lastly, a very simple pragmatic way of setting a desired probe polarization angle is to first rotate the Glan prism so its polarization transmission axis is at right angles to the desired setting. Then, place a white card after the Glan prism and rotate the half-wave plate to whatever setting achieves extinction of the output beam, by visual inspection of the card. The major axis of the polarization ellipse is now at right angles to the transmission axis of the Glan; rotating the Glan back 90 degrees to the desired setting will pass the major axis while extinguishing the minor.

D. LIF Detection: unpolarized and polarized fluorescence detection

The geometrical relationship between the two probe beam directions and the fluorescence imaging region in the drift section of the apparatus is shown in the perspective view of Fig. 2.10. Laser-induced fluorescence is always detected orthogonal to both probe directions by a blue-sensitive photomultiplier tube (PMT) through a series of optics referred to as the PMT “stack”. Although a number of stack configurations were employed throughout the course of this work, in practice, the data presented here were taken with a small number of configurations; the stack was “frozen” into one of these particular configurations for the course of an experiment. While important for both experiments, the stack configuration is particularly crucial for polarized LIF detection used in the rotational alignment experiments. General unpolarized fluorescence detection issues are briefly discussed in Sec. II.D.1; details of polarized fluorescence detection are summarized in Sec. II.D.2.

1. Unpolarized detection

The N_2^+ fluorescence passes through apertures cut into three drift rings at the center of the apparatus (the LIF region). Experimental tests by previous investigators, as well as the *Simion* modeling of Bastian² demonstrate that these cuts make a

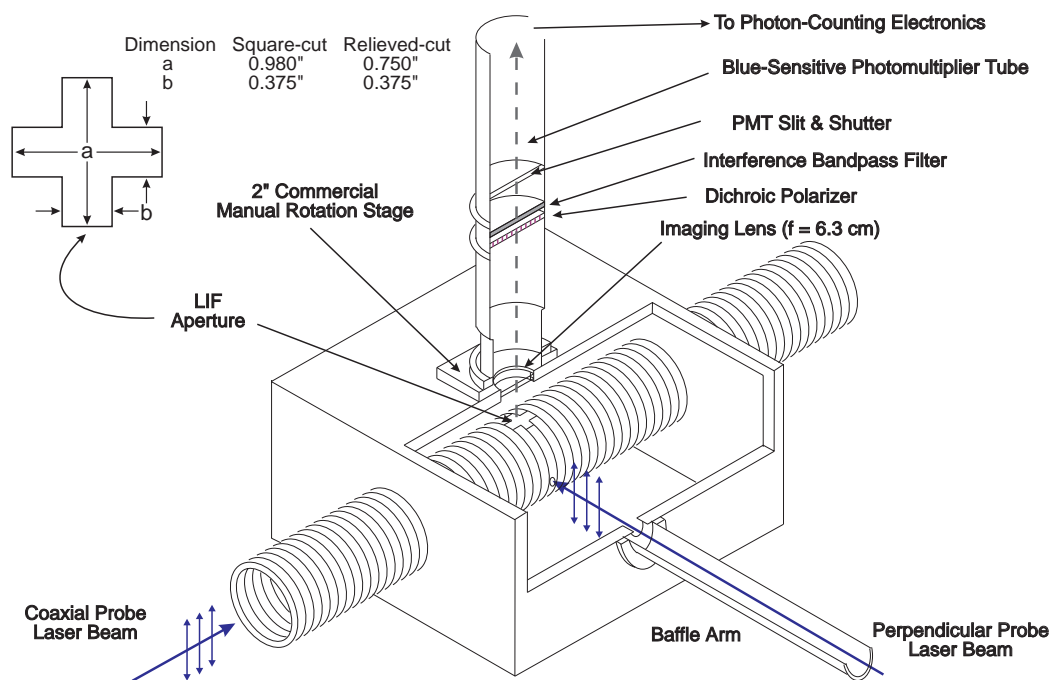


Fig 2.10: Perspective view of apparatus, showing relation between probe beams & LIF detection.

negligible perturbation in electric field uniformity at the LIF region. Two sets of three cut rings were used in practice. The first set, previously employed by other investigators on this project, have a single square-cut opening in the shape of a cross, with dimensions as shown in Fig. 2.10. These rings were used for the first rotational alignment experiments conducted in the Fall of '95. Subsequently, to address a possible LIF polarization systematic in this experiment, these rings were replaced by another set. The new rings have relieved-cut cross-shaped apertures cut into both the top and bottom of the rings. These reliefs were cut to eliminate possible glancing-angle, partially-polarizing fluorescence reflections off of the flat-cut metal surfaces that could be imaged by the PMT. However, diagnostic tests taken with this new set of rings indicate that glancing-angle polarizing reflections off of the surfaces of the original pieces probably made a negligible contribution to the polarization systematic. These relieved-cut rings were employed in both the Fall '97 transport property work and the Spring '98 rotational alignment work.

The LIF then passes through a vacuum window into the light-sealed PMT stack. The LIF windows (Esco Products) used here are made of fused silica. The top window is located 9.0 cm above the drift tube axis and is mounted between two O-rings with an anodized aluminum window holder to minimize possible strain. The window holder has an effective aperture size; two sizes were used in practice. The original window holders had 2.86 cm (1.125 inch) apertures. To narrow down the effective imaging solid angle for the alignment experiments, a second window holder was constructed, with a 1.59 cm (0.625 inch) aperture. Ironically, it now appears that possible polarizing reflections off of the square-cut walls of this aperture piece may have been contributing to the polarization systematic. Two biconvex fluorescence

imaging lenses (Newport) made of BK-7 (one AR coated, one uncoated) and of focal length $f = 6.3$ cm were employed. Although experiments were attempted with the lens at various positions, the best signal-to-background was invariably obtained with the lens as close to the window as possible. The lens focal length was chosen to give approximately 1:1 imaging of the fluorescence in the source region, although this imaging restriction on distances in the PMT stack was not found to be very important in practice.

Even with the most careful production conditions and laser beam alignment, the amount of residual flowing afterglow fluorescence and scattered laser light completely precludes attempting experiments without an interference filter in the fluorescence channel. Two bandpass interference filters were used throughout this work and their transmission functions were characterized on the JILA Cary spectrophotometer. The choice of interference filter for the transport property experiments was somewhat arbitrary and simply based on best signal-to-background. However, for the alignment experiments, it is necessary to know the P/R branch-weighting of the observed fluorescence in order to properly calculate alignment parameters from polarized LIF measurements, as discussed in Sec. IV.B. The filter used for the majority of this work is centered at 431 nm, has a FWHM of 8 nm, and is marked “430 3C NVC-1 5-1”. The interference filter fits into a square-cut “shelf” in a filter assembly that is light-sealed by a half-cylindrical piece of black Delrin plastic.

Only one type of photomultiplier tube was used for this work, the Thorn EMI 9813QB; which is optimized for photon-counting in the blue. The 9813QB has a quartz window leading to an end-on alkali photocathode with an effective cathode diameter of 46 mm and a quantum efficiency of approximately 23% at 425 nm.

Photoelectron multiplication is achieved through 14 beryllium copper dynodes in a linear focused structure with an approximate gain of 7×10^7 . Standard photon-counting biasing networks (Pacific Instruments) for the dynodes are used; the photocathode high-voltage is usually run at -2200 V. The photocathode could be completely shuttered from all fluorescence for a thermionic dark count check, which was particularly important for the alignment experiments. Various 9813QB's will have different dark counts; a tube with a particularly low dark count (serial #4970) was used for most of the experiments conducted. As a final aside, neither the flowing afterglow fluorescence nor the LIF are visible to the naked eye in a darkened room.

2. Polarized detection

For the rotational alignment experiments discussed in Chapter IV, it was necessary to resolve the polarization of the fluorescence. Although other techniques were considered, including the use of a photoelastic modulator in the laser probe beam to modulate the laser polarization, a dual PMT setup with two orthogonal polarizers, and the use of a liquid crystal variable retarder in the fluorescence channel, a very simple fluorescence polarization detection scheme was ultimately chosen. The reasons for using this particular scheme are discussed more fully in Sec. IV.B, and the mechanics of this data acquisition scheme are discussed in Sec. IV.C. Although several different dichroic polarizers were experimented with, in practice a pair of 5.1-cm (2-inch) diameter dichroic polarizers (Optics for Research) with an extinction ratio of better than 10^{-3} were used for all the work presented here.

Several different methods were used to set the angle of the fluorescence polarizer transmission axis. The simplest technique, employed in the earliest alignment experiments, involved mounting the polarizer in a square-cut frame that fits

snugly into one of the shelves of the interference filter assembly, below the interference filter itself. The polarizer transmission axis was indicated to the drift tube axis and firmly taped into place in the frame. To change the polarizer setting, the polarizer frame was rotated 90 degrees and replaced in the stack shelf. This simple method is useful for measuring linear polarization coefficients, which require just two orthogonal polarizer settings; however, this technique suffers from several disadvantages. The primary disadvantage of this method is that it requires breaking the light-seal of the stack for each polarizer rotation. For each rotation, the PMT shutter has to be closed, the black Delrin light seal of the interference filter assembly rotated open, and the polarizer itself rotated, a time-consuming and tedious process. Early diagnostic data indicated that good time correlation between the sequential polarization measurements was essential, so this method was inherently problematic. Additionally, the polarizer setting could not be checked once the light seal was closed, introducing the possibility of operator error in the polarizer rotations.

To address these shortcomings, a slightly more sophisticated approach was taken. A new lens barrel and adapter were built such that the entire PMT stack could be mounted on a commercial 2-inch manually-driven rotation stage (Newport). This particular stack configuration is shown in Fig. 2.10. The interference filter holder assembly is identical to the old stack, and the polarizer is still mounted in one of the shelves, below the filter. However, the entire stack is rotated to set the polarizer transmission axis to a particular angle. The primary advantage of this technique is that the light seal of the PMT stack is not broken for polarizer rotations, greatly speeding the data acquisition. Additionally, the polarizer settings can be checked by the marking on the rotation stage to verify that a clerical error had not been made on a

particular trial. Unfortunately, there are still disadvantages to this method. Although the stage permitted setting the transmission axis of the polarizer to any angle, usually trials were taken at only two angles (0 and 90 degrees) or just a few angles. This scheme required the investigator to manually rotate the stage to the specified angle in the sequence as often as once every eight seconds. These rotations need to be performed repeatedly as rapidly as possible and without clerical error, often for several hours under conditions of considerable duress and fatigue. More importantly, diagnostic data taken with this stack indicated that it was introducing polarization systematics (discussed in Sec. IV.D.1) due to the “wobble” or effective modulation of the detection solid angle as the stack was rotated.

To address these shortcomings, a detection stack was constructed with the polarizer mounted in an integrated rotation stage and driven by a stepper motor. A scale drawing of this stack and stage is shown in Fig. 2.11. The rotation stage is driven by a Geneva mechanism²¹ discretely indexed to 15-degree steps by a detent, which consists of a stainless steel ball constrained by a bushing consisting of four stainless steel rods mounted in a brass sleeve. The stage itself rides on two sets of 2.5 inch i.d. by 3 inch o.d. bearing races (Kaydon). Twenty-four hardened steel pins equally spaced on the diameter of the stage engage both the star wheel of the Geneva mechanism and the ball detent. This design insures that the stage is discretely indexed

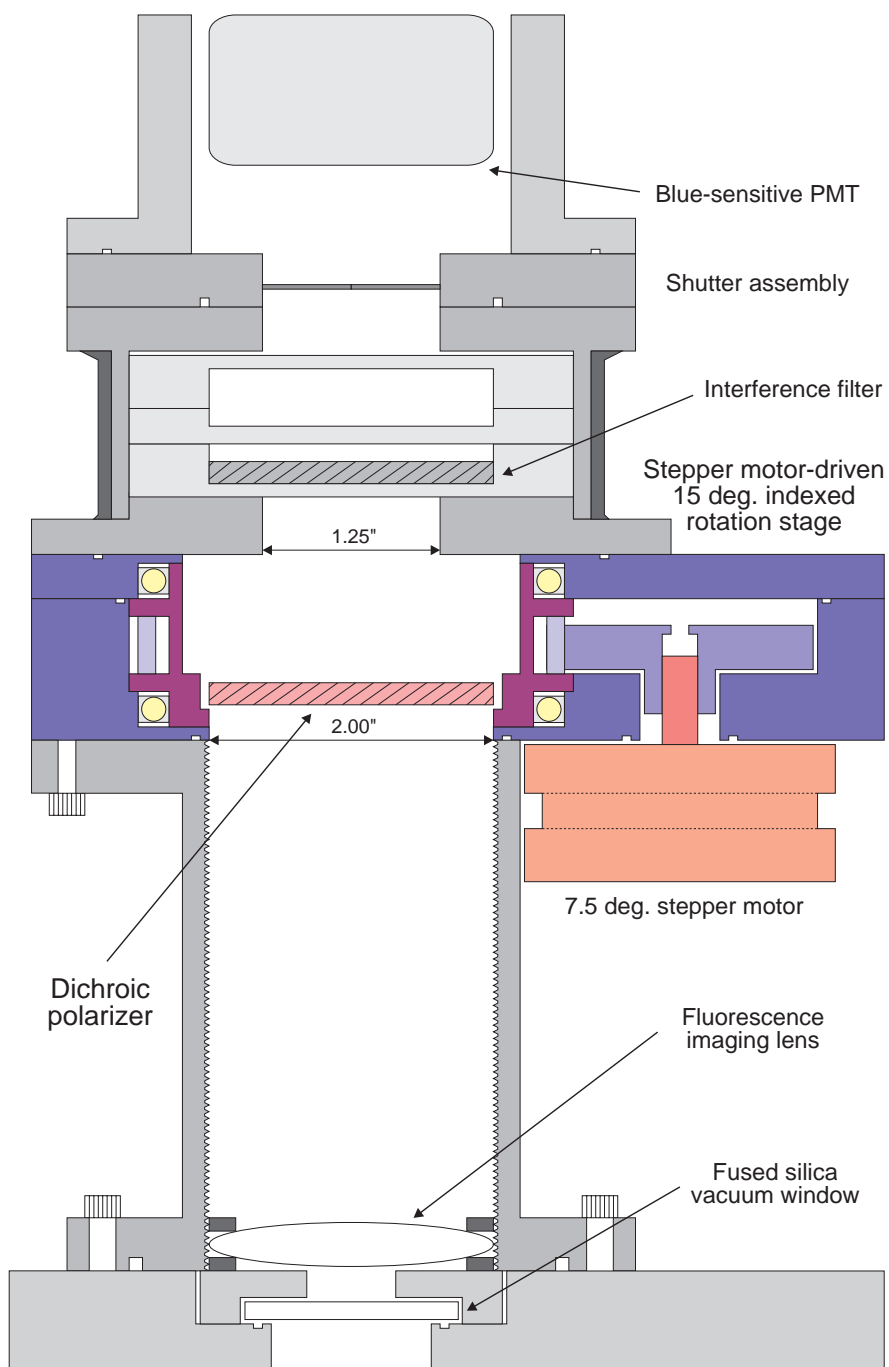


Fig. 2.11: To-scale plan view of stepper-motor driven PMT stack.

to 15 degree steps by the detent and that the stage positioning is completely reproducible; the positioning error is estimated to be less than 0.1 degree. The symmetry of the drift tube means seven distinct polarization angle measurements are possible. The entire assembly is light-sealed so that light seal is never broken to rotate the polarizer. The dichroic polarizer is Torr-Sealed in a 2-inch diameter adapter piece and held in place by three set screws; the stage design permits fine adjustment of the polarizer to match up its transmission axis with the geometry of the apparatus.

A stepper motor is the “torque engine” that drives the stage to a specific detent position. The design goal was to take advantage of the inherent simplicity of stepper motors to produce a system with nearly 100% mechanical reliability. A small stepper motor (Airpax; nominal 5 V, 6.25 ohms/coil) with a 7.5 degree full-step was used for this particular design. The stage is geared such that four stepper motor steps are needed to produce one stage step. A circuit was designed and constructed to drive the stepper motor in the necessary burst mode (schematic in appendix A). The circuit is designed with three inputs from the outside world: a command for a single stage step, which can come from either a front-panel push-button or remotely from a computer, a direction (CW/CCW) flag, and a “Hold/Let go” that effectively shunts the stepper motor coil current, making it impossible for the stage to take a step. This latter feature is crucial, as it was found that just moving around the lab could produce large noise spikes on the stepper motor driver ground plane, triggering a spurious stage step and throwing off the sequencing of the stage. The three inputs are normally driven by digital output signals from the acquisition computer. The fastest reliable operating speed was found to be 75 ms per stage step, or less than 0.5s between 0 & 90 degrees.

The stage is designed to be inherently almost 100% reliable; however, the system is run “open-loop” without verification of angle positioning. An attempt was made to integrate a microswitch into the stage to verify the number of stage steps taken. However, it was found that the microswitch itself would be unreliable unless carefully positioned. Additionally, the drag on the stage caused by the switch made the assembly considerably more unreliable. The simplest and most practical solution was found to be periodically opening the PMT stack at the filter holder and checking the stage position visually. The polarizer sequences were programmed such that the stage was slewed to a “home” position (arbitrarily 0 degrees) between sequences. The stack could then be opened and checked at the sequence boundaries if so desired. The PMT stack was designed to come apart easily in under five minutes at the stage with the PMT shuttered, which permitted “hot” checking of the stack with the PMT voltages still on. Additionally, the stage makes a characteristic chattering noise when slewing, which is noticeably different than the sound produced if it is out of detent. Using the unique acoustic signature of a successful stage step would be the most promising avenue of designing a non-obtrusive closed-loop system for future work.

E. Electronics and data acquisition programming

A brief description is given of the relevant electronics and computer programming issues that arose in the course of the two experiments. The data acquisition is computer-controlled, so these two topics are naturally tied together. All data acquisition programming for both experiments was performed in C (Borland Turbo C 2.01) for a DOS-based computer and integrated into a single program called Eta-Spex. The length of the total program (approximately 13,000 lines with user-interface code and look-up tables) precludes including a print-out; a diskette is

enclosed with the source code in Appendix B. Key features of the program are discussed briefly below. The acquisition programming turned out to be particularly important for the alignment experiment; it was recognized early on that to obtain good statistics, many repetitions would have to be performed of basic acquisition tasks. The philosophy was to use the natural strengths of a computer to handle the clerical and “grunt” repetitive work of the experiment.

All data acquisition in the program is hardware interrupt-driven,²² which means that the user can perform tasks like rescaling the spectra graphics screen or move the graphics cursors while data is being acquired, with the assurance that no data points are being missed. The timing of both the hardware interrupts and counter gates is derived from a 1 MHz crystal, making any timing jitter issues negligible. The program is menu-driven, with the particularly useful feature that numerical parameters such as gate widths are extracted directly from the menu text and not stored in internal look-up tables. Pragmatically, this means a menu parameter can easily be changed and the program recompiled “on the fly” while the experiment is running. The acquisition filename prompting is virtually fool-proof, which insures that files are not lost through operator error. Additionally, the program has filename generation capabilities through a templating mechanism that automatically generates a sequentially numbered filename, which can then be accepted by a single keystroke. This is particularly useful for the transport property experiments, which tend to be file-intensive. The file format is multi-column, tab-delimited ASCII (with a “footer”), which can easily be imported into virtually any data analysis or plotting program.

A block schematic of a portion of the acquisition system is shown in Fig. 2.12. There are three data acquisition and control boards (MetraByte) in the laboratory

computer. A five-counter card based on the AMD 9513 system timing controller²³ is used for event counting; some of the counters are used to gate other counters and trigger interrupts, as shown in the figure. A digital-to-analog (D/A) converter card is used primarily to ramp and position the ring dye laser through external control. The second D/A channel is used to control the programmable floating voltage supply for the experiments discussed in Sec. III.E. An analog-to-digital (A/D) converter card is used to sample the 20 cm ULE Fabry-Perot transmission peaks for the hardware marker positioning method discussed above. Three digital outputs on this card are also used to control the stepper motor-driven rotation stage electronics.

Four event counters of the AMD 9513 are used in the transport property experiments. Counter 5 is tied to a crystal-locked 1 kHz signal, which is used as time base to periodically generate HW interrupts for event counter sampling. The PMT signal was amplified and pulse-height discriminated by a preamp/discriminator (Pacific Instruments) located adjacent to the PMT stack. The PMT pulses are sent to the electronics rack, regenerated by a pulse generator, and sent to a 9513 event counter. A “local” measure of ring dye laser power is derived from either the normalizing photodiode of the cavity-side-lock system or a separate photodiode, as discussed in Sec. II.C. The ring dye laser power signal was always converted into the digital domain by a JILA electronics shop built voltage-to-frequency converter, based on the Raytheon RM4151. It was confirmed that V/F converter used is completely linear over its entire 0-10V range (nominal 1 kHz/V calibration), and always properly

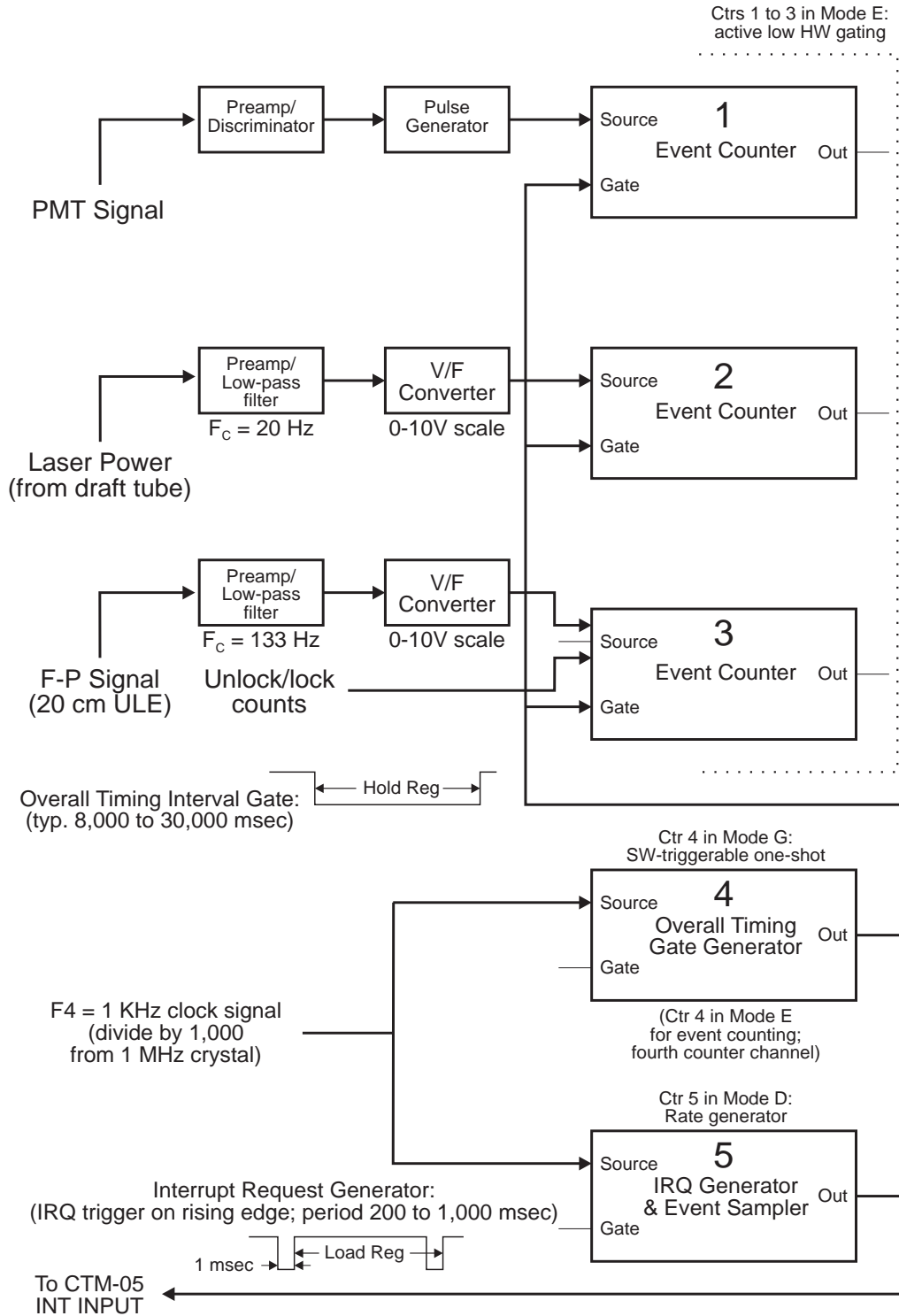


Fig. 2.12: Block schematic of counter portion of acquisition system; the configuration shown is for sub-Doppler alignment experiments.

zero-offset; this detail is particularly important for the alignment experiments because all the LIF signals are laser-power normalized. The Fabry-Perot signals are digitized by two more V/F's and sent to two more event counters. For the sub-Doppler alignment experiments, a slightly different configuration is employed. Three event counters are used; the PMT and laser power signals are treated the same as for the transport property experiment. The third counter receives pulses from the window detector discussed above. Counters 4 and 5 of the 9513 are tied together and used to generate both a hardware gate and periodic sampling interrupt for the event counters. This permits an assessment of the statistical spread in the counting trials to be made.

F. General data analysis considerations

A brief discussion is given of general data analysis issues involved in both experiments. For the transport property experiments, extensive use was made of a commercial non-linear curve fitting program (PeakFit; Jandel Scientific). This program uses the Marquardt-Levenberg algorithm²⁴ to fit a number of library functional forms to user-supplied data. The various functional forms used in this work are discussed in more detail in Chapter III. The fitting program calculates a standard error in the fit for each fit parameter that is subsequently used as a measure of fit uncertainty in the error analysis. The standard errors in the fit parameters are obtained from the covariance matrix \mathbf{C} . Specifically, for a fitting functional form $y(x; \vec{a})$ depending on K fit parameters $a_1..a_K = \vec{a}$, the covariance matrix is defined as $\mathbf{C} = \boldsymbol{\alpha}^{-1}$, with the matrix elements of the matrix $\boldsymbol{\alpha}$ given by²⁴

$$\alpha_{kl} = \sum_{i=1}^N \left(\frac{\partial y(x_i; \vec{a})}{\partial a_k} \right) \left(\frac{\partial y(x_i; \vec{a})}{\partial a_l} \right) \quad (2.13)$$

where the sum runs over the number of data point N . The square roots of the diagonal elements of the covariance matrix multiplied by the square root of the chi-squared per degree of freedom are the standard errors δa_i corresponding to the fit parameters:

$$\delta a_i = \sqrt{\frac{\chi^2}{N_{dof}}} \sqrt{C_{ii}} \quad \text{with} \quad (2.14)$$

$$\chi^2 = \sum_{i=1}^N (y_i - y(x_i; \bar{a}))^2, \quad N_{dof} = N - K$$

The off-diagonal elements of the covariance matrix provide information about how the various parameters are correlated. Although the commercial program does permit user-supplied fitting functions to be used, these functional forms are not pre-compiled, and thus fitting to these forms is agonizingly slow. In the very latter stages of this work, an attempt was made to integrate non-linear fitting routines into Eta-Spex to fit the functional forms discussed in Chapter III to the individual hyperfine components of a line shape. Although this work was not completed, this is the most promising approach for future work. Some basic analysis capabilities were integrated into Eta-Spex. In particular, it was found useful to be able to quickly “page” through and review acquisition files in a particular run. The graphics screen cursors permitted the Fabry-Perot spectrum analysis to be performed visually and thus reasonably quickly. Additionally, since the transport property experiments are file-intensive, some of the diagnostic data (for example, to resolve the axial ion flow systematics) was analyzed “on the fly” by using a Savitzky-Golay²⁵ smoothing routine to smooth the LIF spectrum and then determine the first and second central moments numerically. These numbers (but no file) were then recorded, and the data discarded.

G. Spectroscopy of the $N_2^+ B^2\Sigma_u^+ - X^2\Sigma_g^+$ system

A typical LIF spectra of the $R_1(15)$ spin-rotation line of N_2^+ is shown in Fig. 2.13. Because of both its importance in atmospheric and astrophysical work, and because of the ubiquitous nature of the N_2^+ molecule in plasma environments, its electronic spectroscopy has been quite extensively studied. Additionally, the hyperfine (hf) structure of a number of vibrational bands in the $B^2\Sigma_u^+ - X^2\Sigma_g^+$ system has been studied experimentally. Until quite recently, the hf structure of the $(v', v'') = (0, 0)$ band that this work is concerned with remained unmeasured with sub-Doppler resolution. However, it now appears that high-resolution measurements have been made, and an analysis of this band is underway at the time of this writing.²⁶ Section II.G.1 discusses the general spectroscopic structure of the $B^2\Sigma_u^+ - X^2\Sigma_g^+$ system, while Sec. II.G.2 covers the details of the hyperfine structure.

1. General spectroscopic structure

The general spectroscopic structure of the $^{14}N_2^+ B^2\Sigma_u^+ - X^2\Sigma_g^+$ first negative system is very well known.²⁷ The higher-lying rotational levels ($N'' > 4$) of the ground electronic state are best described by a Hund's case b_{β_J} coupling scheme,²⁸ in which the total orbital angular momentum \mathbf{N} of the electrons and nuclei is added to the unpaired electronic spin angular momentum \mathbf{S} to form \mathbf{J} , which is then added to the coupled nuclear spins \mathbf{I} to form \mathbf{F} , the total angular momentum of the molecule. The presence of a single unpaired electron leads to an electronic spin-rotation splitting of each rotational line N into two spin doublets with resulting J values $J_1 = N + \frac{1}{2}$ and

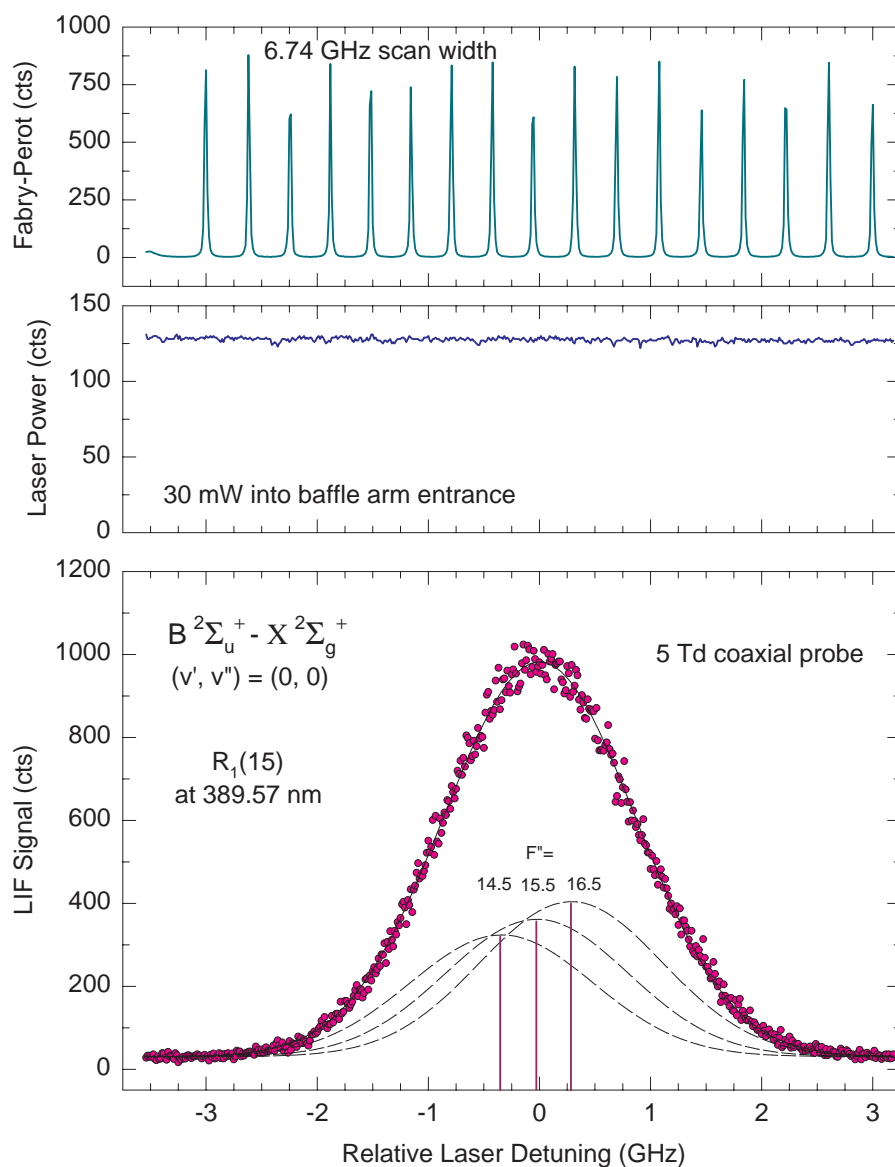


Fig. 2.13: Typical LIF spectra of a single spin-rotation line, illustrating the Doppler-broadened, unresolved hyperfine structure. Three Gaussians of equal linewidth are placed on each of the components in the stick spectra.

$J_2 = N - \frac{1}{2}$. Each of these spin-rotation levels is further split by nuclear spin interactions into either (effectively) five or three hyperfine levels, depending on the symmetry of the rotational level. Each ^{14}N nucleus is a boson with spin 1; these spins couple together to give a total nuclear spin of $I = 0, 1, \text{ or } 2$. The requirement that the total wavefunction of the molecule be symmetric under interchange of the nuclei leads to even N'' rotational levels associated with $I = 0$ or 2 for a total of six hyperfine components, two of which are nearly degenerate. The odd N'' rotational levels are associated with $I = 1$ and have three non-degenerate hyperfine components. The familiar 2:1 even/odd N'' intensity alternation of the rotational spectrum of N_2^+ is a consequence of these spin statistics. The consequence for the dynamics is that there are two non-interacting rotational manifolds, the ortho (N'' even) or para (N'' odd) states, which leads to an effective doubling of the rotational constant for the spacing of adjacent rotational levels within a given manifold.

Figure 2.14 shows this general spectroscopic structure for the $\text{R}_1(15)$ LIF transition, with the dominant radiative transitions obeying the propensity rule $\Delta F = \Delta J = \Delta N = \pm 1$. Since the spin-rotation splitting of the spin doublet varies as γN , with an effective spin-rotation constant $\gamma_{v''=0} = 272.8 \text{ MHz}$,²⁹ the J_1 and J_2 branches can be easily resolved by the resolution of this experiment. Figure 2.15 shows 0 Td LIF survey spectra of five rotational lines in the para manifold. Note that the wings of the lines begin to overlap around $N''=7$. Table 2.1 gives the relevant rest transition frequencies for the lines studied in this experiment, as calculated from a standard Dunham expansion³⁰ with known molecular constants.

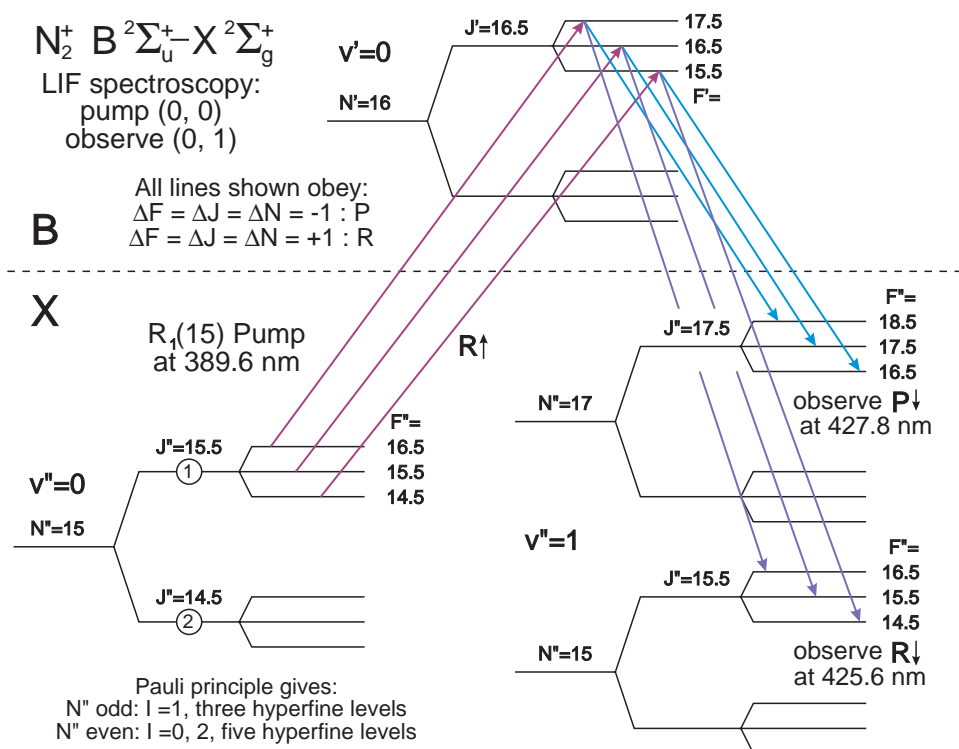


Fig 2.14: Pump-fluoresce diagram for $R_1(N''=15)$, showing typical spectroscopic structure for para manifold.

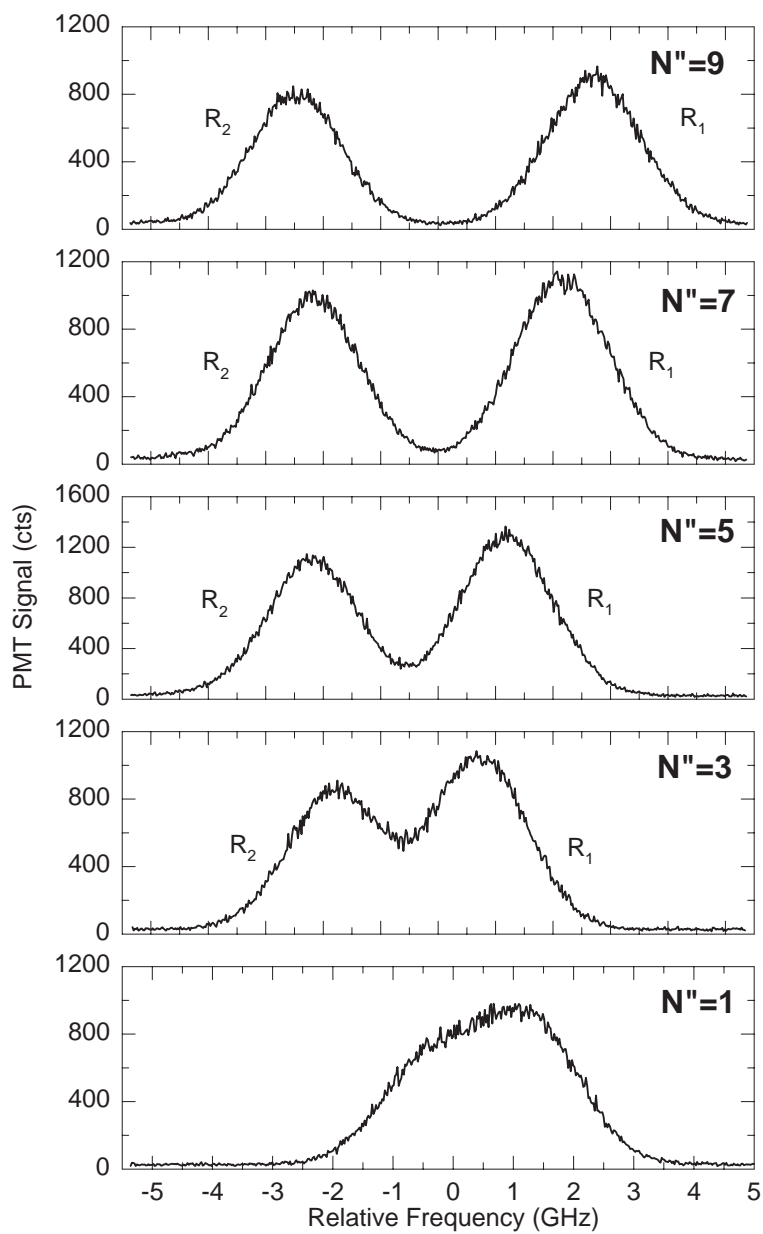


Fig. 2.15: LIF survey spectra of five lines in the para manifold. Data were taken at 0 Td with perpendicular laser probe.

Transition	J''	$\bar{\nu}_0$ (cm ⁻¹)	λ_0 (nm)
R ₂ (3)	2.5	25,584.38	390.863
R ₁ (3)	3.5	25,584.46	390.862
R ₂ (9)	8.5	25,621.12	390.303
R ₁ (9)	9.5	25,621.28	390.301
R ₂ (10)	9.5	25,628.31	390.194
R ₁ (10)	10.5	25,628.48	390.191
R ₂ (11)	10.5	25,635.80	390.079
R ₁ (11)	11.5	25,635.99	390.077
R ₂ (12)	11.5	25,643.60	389.961
R ₁ (12)	12.5	25,643.80	389.958
R ₂ (13)	12.5	25,651.70	389.838
R ₁ (13)	13.5	25,651.92	389.834
R ₂ (14)	13.5	25,660.11	389.710
R ₁ (14)	14.5	25,660.34	389.706
R ₂ (15)	14.5	25,668.82	389.578
R ₁ (15)	15.5	25,669.07	389.574
R ₂ (16)	15.5	25,677.83	389.441
R ₁ (16)	16.5	25,678.10	389.437
R ₂ (17)	16.5	25,687.16	389.300
R ₁ (17)	17.5	25,687.44	389.295
R ₂ (18)	17.5	25,696.78	389.154
R ₁ (18)	18.5	25,697.08	389.149
R ₂ (19)	18.5	25,706.71	389.003
R ₁ (19)	19.5	25,707.02	388.999
R ₂ (20)	19.5	25,716.95	388.849
R ₁ (20)	20.5	25,717.27	388.844
R ₂ (21)	20.5	25,727.49	388.689
R ₁ (21)	21.5	25,727.83	388.684
R ₂ (22)	21.5	25,738.33	388.526
R ₁ (22)	22.5	25,738.69	388.520

Table 2.1: Relevant rest transition frequencies for the R-branch of the (0,0) band of the $N_2^+ B^2\Sigma_u^+ - X^2\Sigma_g^+$ system, as calculated from a Dunham expansion.

2. Hyperfine spectroscopy

There is unresolved Doppler-broadened hyperfine structure underlying each of the spin-rotation branches, as shown in Fig. 2.13. For optical transitions, the hyperfine interaction is primarily due to the magnetic interaction of electronic and nuclear spins. The energy spacing of the hyperfine components has been well-studied for the $(v', v'') = (0, 1)^{31, 32}$ and $(1, 2)^{33}$ bands of $^{14}\text{N}_2^+$ by the technique of fast ion-beam laser spectroscopy, which permits kinematic compression of the hyperfine Doppler widths to less than 100 MHz. Somewhat surprisingly, it appears that precise spectroscopic magnetic hyperfine parameters for $v'' = 0$ have not previously been measured or calculated. In particular, the Fermi contact interaction coupling constant b_F and the dipole interaction coupling constant t are necessary to calculate the needed matrix elements. A simple linear extrapolation of the known b_F'' and t'' coupling constants for $v'' = 2$ and 1 gives an estimate of $b_F'' \approx 90$ MHz and $t'' \approx 20$ MHz. It might be anticipated that these magnetic hyperfine parameters would depend quite sensitively on the structure and extent of the $v'' = 0$ electronic wavefunction in the vicinity of the ^{14}N nuclei and that using the known (0,1) spectroscopy could lead to significant error. However, most of the hf splitting observed in optical transitions in the (0,0) and (0,1) bands is actually due to splitting in the upper ($B, v' = 0$) state, common to both $v'' = 0$ and $v'' = 1$, due to its considerably larger Fermi coupling constant.²⁶

Thus, throughout this work, we approximate the $v'' = 0$ hf spectroscopy with the known $v'' = 1$ spectroscopy. Specifically, we use the tabulated $v'' = 1$ hf

spacings³² for each rotational transition probed; these spacings are approximately 0.01 cm^{-1} (0.3 GHz), and fairly independent of rotational state. For the relative hyperfine intensities within a spin-rotation line, explicit intensity formulas can be worked out, starting from the assumption that the individual hf intensities vary as the product of the square of two dipole reduced matrix elements

$$I(F_i) \propto \left| \langle F_f \| r^{(1)} \| F_e \rangle \langle F_e \| r^{(1)} \| F_i \rangle \right|^2 \quad (2.15)$$

The conventional basis kets for Hund's case b_{β_J} coupling are $|\gamma N S J I F M_F\rangle$. Noting that the dipole operator acts only on the spatial angular momentum N and not on the spin degrees of freedom I and S , repeated use of the identity³⁴

$$\begin{aligned} \left| \langle \gamma (J I) F \| r^{(1)} \| \gamma' (J' I) F' \rangle \right|^2 = \\ (2F+1)(2F'+1) \left\{ \begin{matrix} J & F & I \\ F' & J' & 1 \end{matrix} \right\}^2 \left| \langle \gamma J \| r^{(1)} \| \gamma' J' \rangle \right|^2 \end{aligned} \quad (2.16)$$

for both the I and S couplings will decompose the reduced matrix elements and produce explicit algebraic formulas for the relative intensities of hf transitions within a spin-rotation line. However, the algebraic formulas³⁵ are too lengthy to include here. As mentioned above, an accurate sub-Doppler measurement of the hyperfine spectroscopy of the $(\nu', \nu'') = (0,0)$ band has now been performed, and this analysis is the most promising avenue for future work.

References for Chapter II

1. T. S. Zwier, Ph. D. Thesis, University of Colorado (1981).
2. M. J. Bastian, Ph. D. Thesis, University of Colorado (1994).
3. A. L. Schmeltekopf, E. E. Ferguson, and F. C. Fehsenfeld, *J. Chem. Phys.* **48**, 2966 (1968).
4. A. L. Schmeltekopf and F. C. Fehsenfeld, *J. Chem. Phys.* **53**, 3173 (1970).
5. J. H. Kolts and D. W. Setser, in *Reactive Intermediates in the Gas Phase*, edited by D. W. Setser (Academic Press, New York, 1979).
6. M. A. Smith, Ph. D. Thesis, University of Colorado (1982).
7. C. E. Hamilton, Ph. D. Thesis, University of Colorado (1985).
8. E. E. Ferguson, F. C. Fehsenfeld, and A. L. Schmeltekopf, *Adv. At. Mol. Phys.* **5**, 1 (1969).
9. D. Smith and N. G. Adams, in *Gas Phase Ion Chemistry, Vol. 1*, edited by M. T. Bowers (Academic Press, New York, 1979).
10. E. A. Mason and E. W. McDaniel, *Transport Properties of Ions in Gases* (John Wiley & Sons, New York, 1988).
11. J. Bergquist, private communication (1996); see also A. Steinbach, M. Rauner, F. C. Cruz, and J. C. Bergquist, *Opt. Commun.* **123**, 207 (1996).
12. R. M. Williams, Ph. D. Thesis, University of Colorado (1997).
13. T. F. Johnston, R. H. Brady, and W. Proffitt, *Appl. Opt.* **21**, 2307 (1982).
14. T. F. Johnston, Jr., article "Tunable Dye Lasers" in *Encyclopedia of Physical Science and Technology*, Vol. 14 (Academic Press, Orlando FL, 1987).
15. L. Hollberg, in *Dye Laser Principles with Applications*, edited by F. J. Duarte and L. W. Hillman (Academic Press, Boston, 1990) Chap. 5.
16. F. P. Tully and J. L. Durant, Jr., *Appl. Opt.* **27**, 2096 (1988).
17. T. Johnston, *Opt. Commun.* **69**, 147 (1988).
18. A. E. Siegman, *Lasers* (University Science Books, Mill Valley, CA, 1986).

19. Corning Code 7971 mirror-grade ULE; purchased from United Lens Company, Southbridge MA (508) 765-5421.
20. L.-S. Ma , J. Ye and K. Vogel, private communication (1996).
21. D. Alchenberger, private communication (1997). David Alchenberger of JILA Instrument Shops was primarily responsible for the design and construction.
22. E. B. Anthony, undergraduate thesis, Middlebury College (1987).
23. Advanced Micro Devices, *Am 9513A/Am 9513 System Timing Controller Technical Manual* (Advanced Micro Devices, Inc., Sunnyvale CA, 1985).
24. W. H. Press, B. P. Flannery, S. A. Teukolsky, and W. T. Vetterling, *Numerical Recipes in C: The Art of Scientific Computing* (Cambridge University Press, Cambridge, 1988).
25. A. Savitzky and M. J. E. Golay, *Anal. Chem.* **36**, 1627 (1964).
26. S. D. Rosner, private communications (1997, 1998).
27. A. Lofthus and P. H. Krupenie, *J. Phys. Chem. Ref. Data* **6**, 113 (1977).
28. C. H. Townes and A. L. Schawlow, *Microwave Spectroscopy* (McGraw-Hill, New York, 1955).
29. T. A. Miller, T. Suzuki, and E. Hirota, *J. Chem. Phys.* **80**, 4671 (1984).
30. J. I. Steinfeld, *Molecules and Radiation: An Introduction to Modern Molecular Spectroscopy*, 2nd ed. (MIT Press, Cambridge MA, 1985).
31. N. B. Mansour, C. Kurtz, T. C. Steimle, G. L. Goodman, L. Young, T. J. Scholl, S. D. Rosner, and R. A. Holt, *Phys. Rev. A* **44**, 4418 (1991).
32. T. J. Scholl, A. W. Taylor, R. A. Holt, and S. D. Rosner, *J. Mol. Spectrosc.* **152**, 398 (1992).
33. K. Boudjarane, J. Lacoursiere, and M. Larzilliere, *J. Chem. Phys.* **101**, 10274 (1994).
34. R. N. Zare, *Angular Momentum: Understanding Spatial Aspects in Chemistry and Physics* (Wiley-Interscience, New York, 1988); see pp. 194-195, Eqs. (5.68) & (5.72).
35. E. B. Anthony, private calculation (1994).